Electronic Supplementary Information: Mechanistic studies of the photo-electrochemical hydrogen evolution reaction on poly(2,2'-bithiophene)

Chun Hin Ng,[*a] C. André Ohlin,[b] Siyao Qiu,[b] Chenghua Sun[b] and Bjorn Winther-Jensen[a]

November 26, 2015

1   Effect of Fe(II/III) ions on catalysis

A key concern that needed to be addressed was the issue of residual Fe^{2+}/Fe^{3+} oxidant after the ethanol wash step. It has been recognised that trace amounts of metal calatyst particles have been able to bring about a significant catalytic response despite being in the concentrations of ppm. Thus it became critical to determine whether our photo-electrocatalytic activity was an inherent property of PBTh or if it was a result of trace Fe particles (or a combination of the two).

For the investigation, four films of PBTh were washed in different solutions after polymerisation with the aim to discern differences in performance according to the effectiveness of Fe^{3+} removal. The initial wash solutions were: H_2O, ethanol, $0.1\,mol\,L^{-1}$ para-toluenesulphonic acid (PTSa) in H_2O (pH = 0.9) and $0.1\,mol\,L^{-1}$ PTSa in ethanol. It was assumed that the hydrophobic nature of PBTh would reduce the penetration of aqueous media, thus ethanol would be more effective at removing Fe species than H_2O. At the same time, Fe^{2+}/Fe^{3+} species are more soluble in acidic media, hence the acidic $0.1\,mol\,L^{-1}$ PTSa solutions should remove more Fe than their neutral counterparts.

After the initial wash, each film was tested via CA (at $-0.8\,V$ vs Ag/AgCl) in $0.1\,mol\,L^{-1}$ PB (pH 7) to compare their photo-electrocatalytic performance (Figure S1A). A cursory analysis of this result shows significantly higher photo-currents from the acidic wash solutions, however a proper quantification of the Fe in the films was required. To this end, the four films were then washed in $0.1\,mol\,L^{-1}$ PTSa in H_2O after CA testing, and the resulting wash solution collected. Peroxide was added to each film's wash solution to convert Fe^{2+} to Fe^{3+}, followed by KSCN to form the $FeSCN^{2-}$ complex. The Fe^{3+} content of each of the four wash solutions was then determined by analysing the UV-Vis absorption peak of the resulting $FeSCN^{2-}$ ion at 460 nm. This analysis is referred to as the "initial wash".
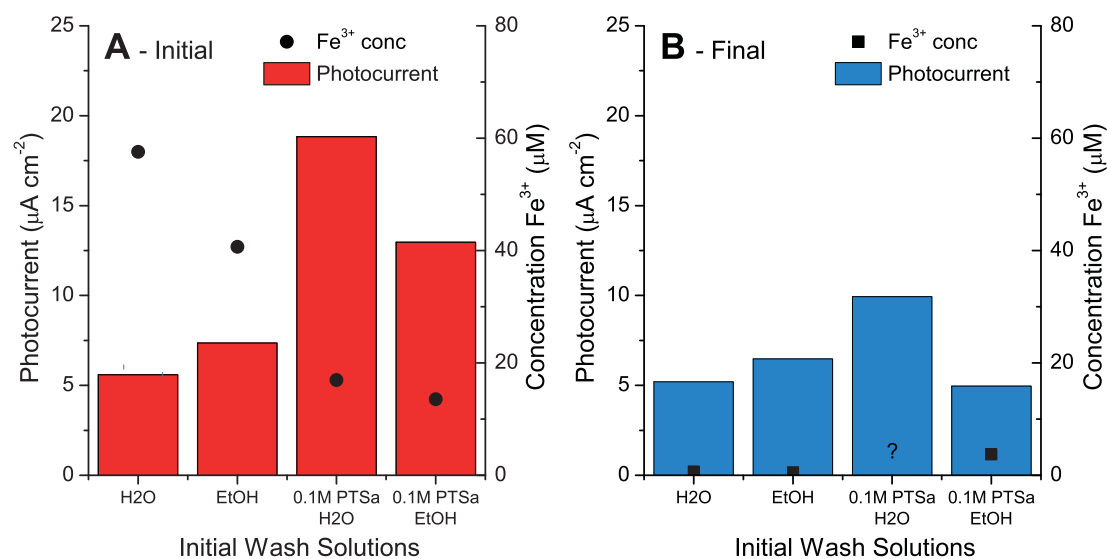
Figure S1: Comparison of the photocurrent obtained via CA at $-0.8\,\mathrm{V}$ vs Ag/AgCl **A:** after the initial wash, and **B:** after the 6 acid washes to remove Fe^{3+}. The detected Fe^{3+} concentration in the wash solution ($0.1\,\mathrm{mol\,L^{-1}}$ PTSa in H_2O) after each test is also shown (in black). The Fe^{3+} concentration of the 0.1M PTSa H_2O in the final wash was not detectable.

The calculated Fe^{3+} concentration from each sample (of the initial wash) is presented in Figure S1A as the • markers and show an inverse relationship between the amount of residual iron and catalytic performance (photocurrent). This supports our case that iron does not play a role in the catalysis process and in fact, it seems that having more residual iron in the system is *detrimental* to catalytic performance.

In an attempt to completely remove any traces of Fe, the four films were subjected to a series of washes in $0.1\,\mathrm{mol\,L^{-1}}$ PTSa in H_2O and Ethanol. At each step, the wash solution for each film was collected and analysed for their iron content which showed a reduction in Fe concentration of up to three orders of magnitude from the initial wash to wash 7, Figure S2. Washes 5 and 6 had a higher concentration of Fe^{3+} though this can be explained by the use of ethanol; where the enhanced penetration of ethanol into the bulk film enabled the release of previously trapped Fe species. The final wash back in the aqueous $0.1\,\mathrm{mol\,L^{-1}}$ PTSa solution revealed that the Fe concentration had indeed further decreased.

After wash 6, the films were tested again for their photo-electrochemical performance and showed photocurrents that were on par with that of the initial tests, despite having significantly lower concentrations of Fe, see Figure S1B. There are decreases in catalytic performance for all samples after the six wash steps, however, this is more likely to be caused by delamination of the film from the FTO substrate and mechanical damage from the successive swelling and drying processes involved in each wash step rather than from the difference in iron concentration. This is especially apparent when considering the PBTh sample that was initially washed with H_2O.
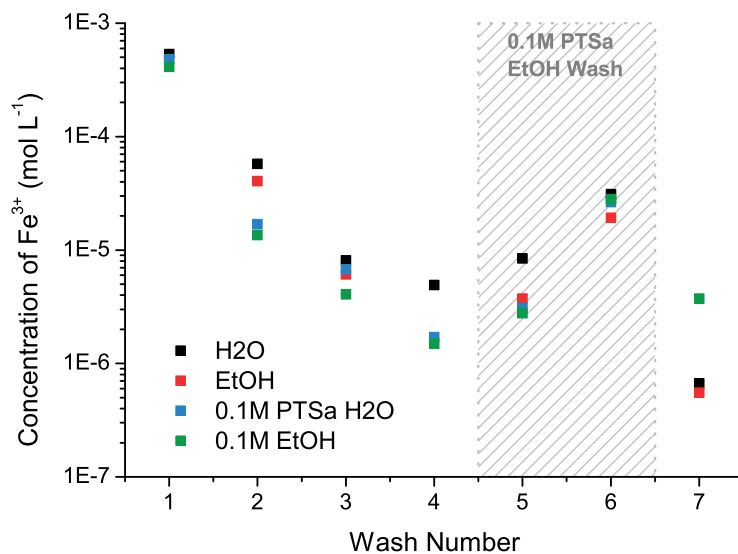
Figure S2: The detected concentration of Fe^{3+} from UV-Vis spectroscopy after each successive wash step. Wash 1 utilised the initial varying wash solutions; thereafter, wash 2-4 and wash 7 used 0.1 M PTSa in H_2O and wash 5-6 used 0.1 M PTSa in EtOH. Certain data points were unavailable due to saturation of the UV-Vis detector or difficulty in resolving the $FeSCN_2^-$ peak.

The catalytic performance is almost completely unaffected despite the three order of magnitude decrease in Fe concentration (from $534\,\mu mol\,L^{-1}$ at the initial wash to $0.7\,\mu mol\,L^{-1}$ at the 7th wash). This provides compelling evidence that catalytic behaviour is not dependent on entrapped iron particles and in fact, the presence of Fe seems to impair catalytic performance.

2 In-situ Raman Spectroscopy

2.1 Set-up

Further information on the in-situ Raman spectroscopy experiments are provided. Figure S3 show the experimental set-up, efforts were made to limit the ingress of air using heavy N_2 purging but O_2 contamination from the atmosphere remain an issue for consideration.
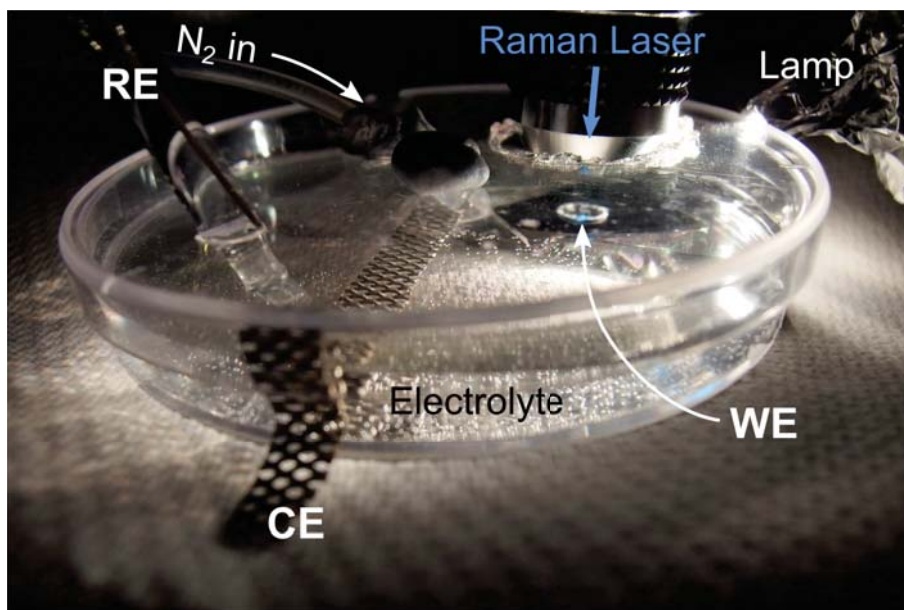

Figure S3: The in-situ Raman set-up showing the electrochemical electrodes and how the cell was arranged. N_2 was purged into the headspace above the electrolyte throughout the experiment to remove as much air as possible.

2.2 Assigning the Raman peaks at 2160 and 2500cm^{-1}

The observed peaks at 2160 and $2500\,\text{cm}^{-1}$ were not easily assigned. However, given the inertness of the peaks to changes in illumination, potential and electrolyte, it was assumed to be independent of the photo-electrocatalytic process. This is further supported by the presence of similar peaks in sexithiophene, an indication that these peaks are inherent to oligothiophene, not a reaction intermediate (see ESI†, Figure S7). Possibly due to an interaction between adjacent PBTh chains.

A comparison of the dry sexithiophene (obtained from Signam Aldrich) and PBTh Raman spectrum is presented in Figure S4. Despite our best efforts, we could not reduce the fluorescence from sexithiophene. Nonetheless, comparison of these Raman spectra shows that the presence of the peaks at 2160, 2500 and $2900\,\text{cm}^{-1}$ are not indicative of a reaction intermediate.
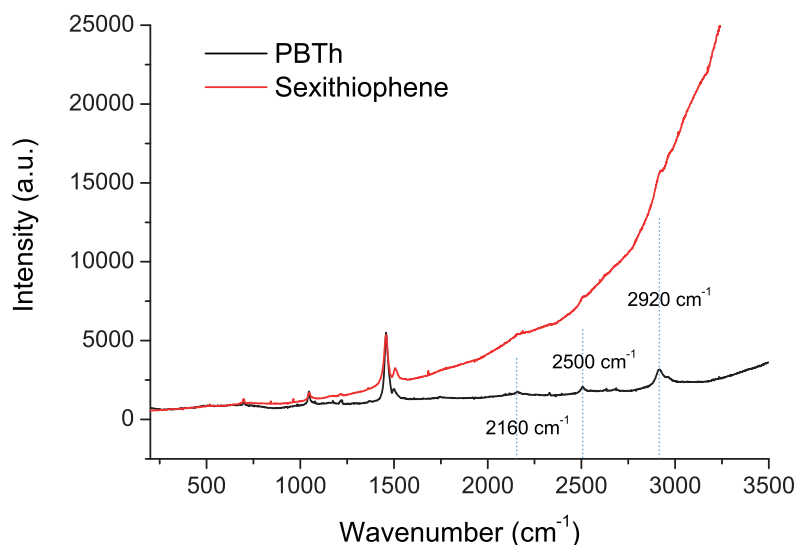
Figure S4: Comparison of the PBTh Raman spectra with sexithiophene.

2.3 Catalysis from the 488 nm laser

The issue of the blue 488 nm Raman laser triggering the catalytic reaction is highlighted in Figure S5A. Even with no external light source, a catalytic photo-current was recorded with application of the Raman laser; this effect from the blue laser is even observable with the external lamp. By comparison, the red 633 nm HeNe laser had no effect on the photo-catalytic response, Figure S5B. The increase in CA current during illumination was attributed to the swelling of the film as H_2 was produced.

2.4 Raman studies in H_2SO_4

As an experiment to probe extreme reduction conditions, in-situ Raman was conducted in $1 \, mol \, L^{-1}$ H_2SO_4 (pH 0) with the 488 nm laser. In an attempt to limit background interference from external light sources, only the applied electrochemical potential and the blue Raman laser was used to activate the reduction reaction . Two potentials were applied, 0.6 V and -1.2 V vs Ag/AgCl, and the resulting spectra is shown in Figure S6 along with the blank H_2SO_4, dry PBTh and wet PBTh (E_{oc}) background spectra.

As with previous in-situ tests, the Raman spectra in H_2SO_4 did not reveal the formation of extra peaks or any significant chemical shifts with applied potential. Once again, the sole distinguishing feature between the spectra was the increase in fluorescence with more negative potentials. The small peak at $985 \, cm^{-1}$ was originally thought to correspond to a S—H intermediate state, especially since S—H bending modes have been known to be observed between $800–1000 \, cm^{-1}$. This was particularly exciting since a similar band was also observed
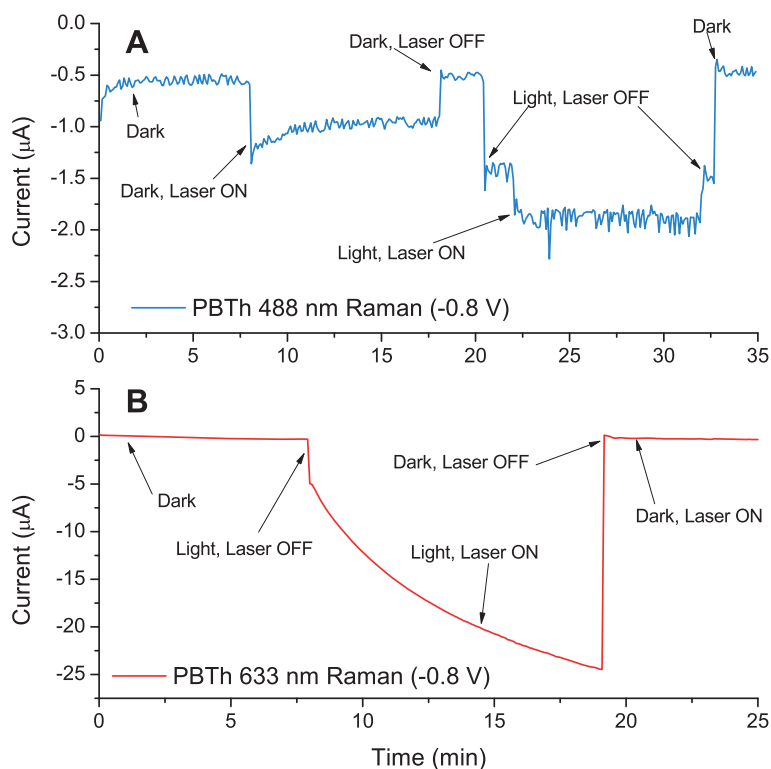
5

Figure S5: A: The CA trace of PBTh for in-situ Raman in the blue (488 nm) laser whilst held at -0.8 V vs Ag/AgCl in $0.1\,\text{mol}\,\text{L}^{-1}$ PB, pH 7. As the figure shows, the blue laser was sufficient to generate a substantial photo-catalytic response and makes determination of the "dark" PBTh Raman spectrum impossible. **B:** The CA trace of PBTh whilst running in-situ Raman with the 633 nm laser; photo-excitation is only triggered when the external light was switched on.

in PB (In main text, Figure 5B, red trace at $\approx 990\,\text{cm}^{-1}$). However, this peak is present in both the H_2SO_4 and PB blank and moreover, is directly proportional to electrolyte concentration; see Figure S7. This thus emphatically rules out a S—H intermediate state as a possible candidate.
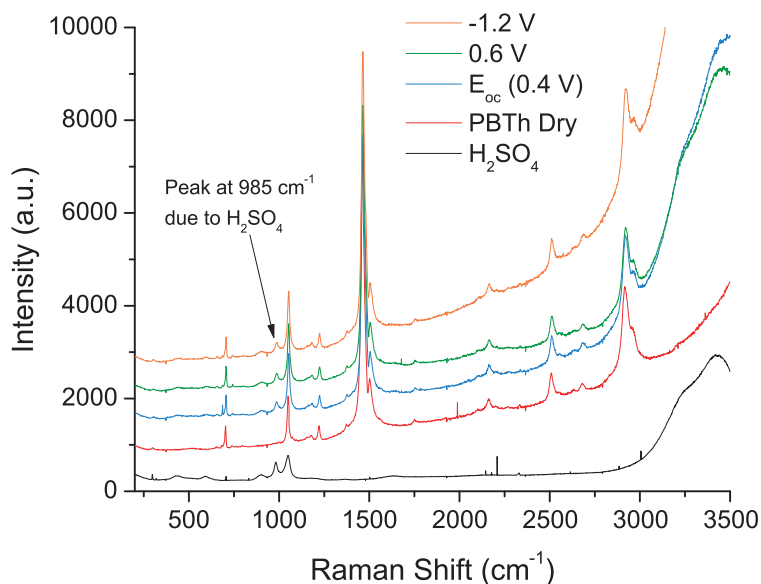
Figure S6: The Raman spectra of PBTh under an applied potential of $0.6\,\mathrm{V}$ and $-1.2\,\mathrm{V}$ is shown; conducted in $1\,\mathrm{mol\,L^{-1}}$ H_2SO_4 (pH 0) and with $488\,\mathrm{nm}$ Raman laser as the sole light source. The baseline spectra of H_2SO_4, dry PBTh and wet PBTh at the open circuit potential ($E_{oc} = 0.4\,\mathrm{V}$) is also given for comparison.
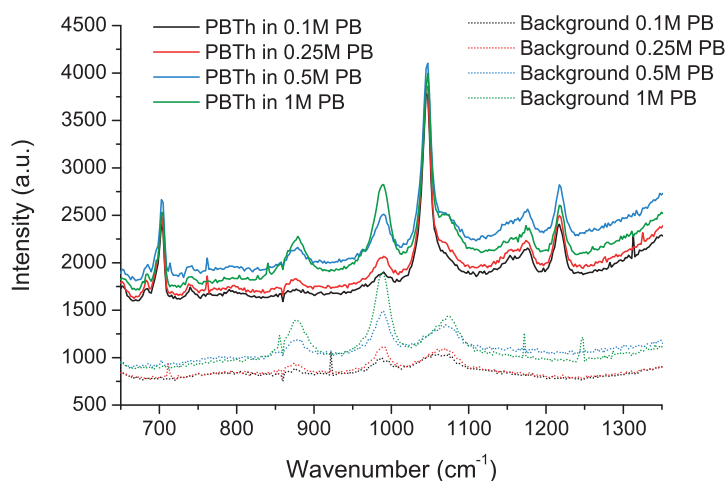

Figure S7: Raman spectra of PBTh in various concentrations of phosphate buffer (pH 7) compared with the background phosphate buffer spectra. The PBTh spectra have been offset for clarity.

3 In-situ UV-Vis spectroscopy

In-situ UV-Vis spectroscopy was used in an attempt to probe the changes in the electronic band structure which was thought to occur by the protonation of the PBTh chain and the subsequent change of the π-electron conjugation. This idea was supported through time-dependent density function theory (TD-DFT) calculations.

From TD-DFT, it was observed that the protonation of a 7-membered thiophene oligomer to PBTh(S-H)$^+$ led to a substantial change in the overall absorption spectra, see Figure S8. Thus it was hoped that by probing the in-situ appearance and disappearance of the predicted PBTh(S-H)$^+$ absorbance peaks (at $\approx 650\,$nm), insight into the mechanism could be gained. For comparison, the TD-DFT predicted absorbance of a 7-membered thiophene oligomer as well as the experimental absorption spectrum of PBTh are also provided. The good correlation between the theoretical and observed spectra provides support that our modelling methods are suitable.
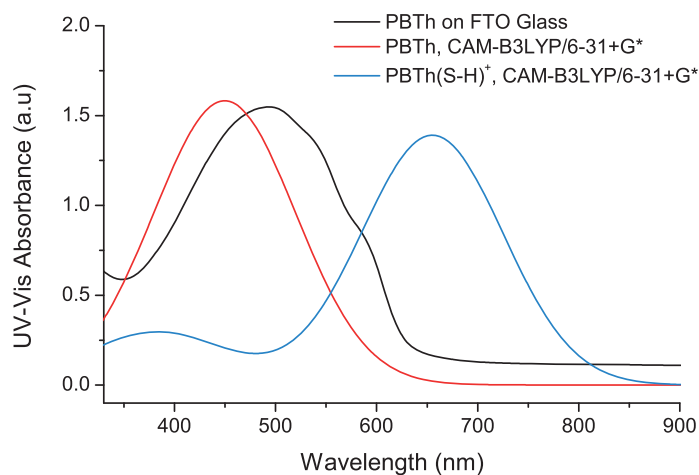

Figure S8: The predicted UV-Vis absorbance spectrum of PBTh and the expected PBTh(S-H)$^+$ intermediate as modelled by TD-DFT. The experimental UV-Vis absorption spectrum of PBTh is also presented.

For the in-situ measurements, a standard PBTh film was polymerised onto FTO glass and placed in the metal cell setup. UV-Vis absorption spectroscopy was conducted whilst applying potential in an electrolyte of $0.1\,\mathrm{mol\,L^{-1}}$ PB, pH 7. The utmost care was taken to shield the detector from stray light but significant background scattering caused saturation of the UV-Vis spectrometer at all but the lower photo-intensities; examples can be seen in Figure S9. A more recognisable spectrum was obtained at the lower intensities of 0.05 and 0.03 sun and is shown in Figure S10A. While it avoids the saturation of the detector, there is negligible photo-effect and still considerable noise. The increase in absorbance at $850\,$nm and $350\,$nm is likely the result of scattering from the change in diffraction grating and absorption from the

FTO substrate respectively. A Logitech R800 green laser pointer 522 nm was also used in an attempt to reduce interference but it was unable to sustain a consistent beam output.
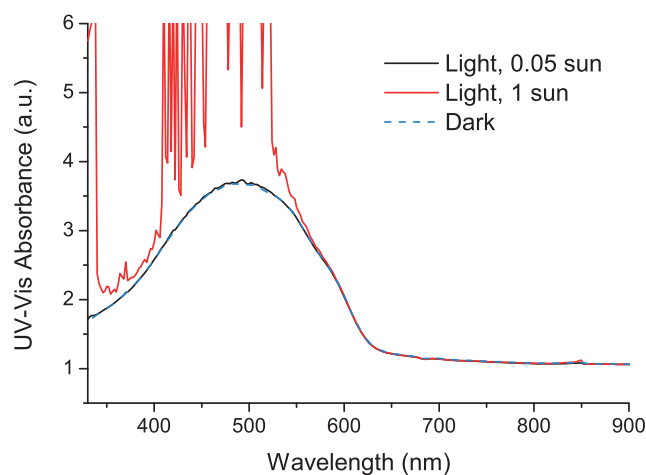

Figure S9: The UV-Vis spectra when light is shone onto the film whilst holding at 0.6 V in 0.1 mol L^{-1} PB, pH 7; the dark absorption spectrum of PBTh is also included.

The absence of the expected PBTh(S-H)$^+$ peak at ≈ 650 nm suggests that these species are either short-lived, low in population, a combination of the two, or are simply not formed. Given the difficulties in the effective photo-activation of the PBTh film however, their absence was not surprising and does not provide conclusive evidence without more reliable measurements.
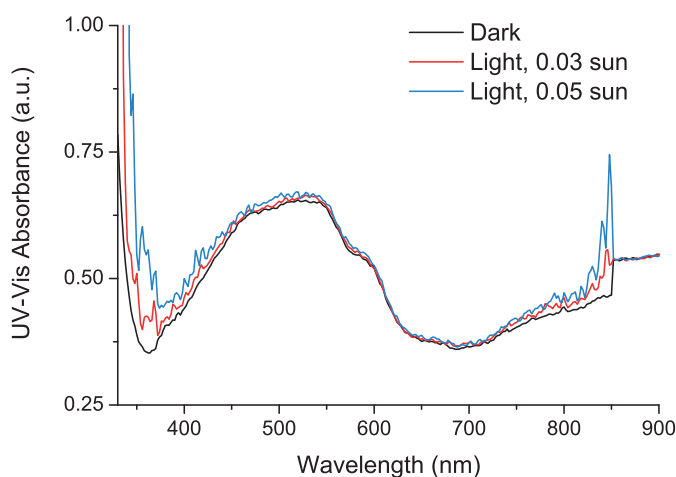

Figure S10: UV-Vis of the PBTh on FTO glass in dark and light (different intensities) whilst held at -0.8 V vs Ag/AgCl.

4 Extended Cyclic Voltammetry of PBTh

The need to apply electrochemical potential and photo-illumination complicates many spectroscopic methods. In recognition of this, an attempt to trigger the HER catalysis via electrochemical potential alone was made. An extended CV of PBTh was performed with an applied reduction potential of up to $-1.8\,V$ vs Ag/AgCl and shown in Figure S11. This extended CV shows the catalytic performance of PBTh to the HER in light and dark (in $0.1\,mol\,L^{-1}$ PB, pH 7) as well as its self-reduction and oxidation reactions in anhydrous PC (Figure S11, blue trace).
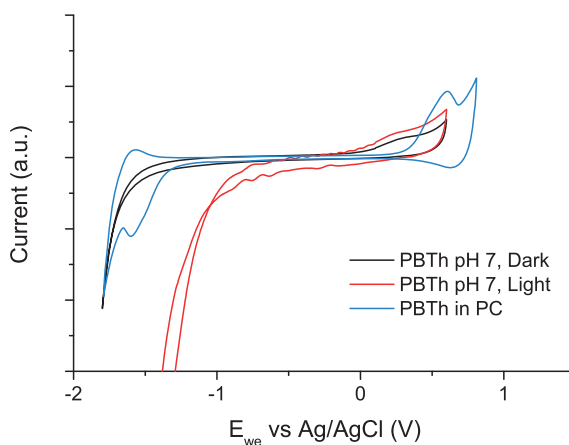

Figure S11: An extended CV of the PBTh film showing the electrochemical behaviour in aqueous $0.1\,mol\,L^{-1}$ PB at pH 7.0 and in anhydrous PC ($0.1\,mol\,L^{-1}$ TBAPF$_6$) whilst under N$_2$; no differences were observed between light and dark in PC.

As expected, the application of light triggered the photo-electrocatalytic response from PBTh in the aqueous electrolyte, but a strong reduction tail was also observed on PBTh in dark (Figure S11, black) with an onset of ca. $-1.5\,V$ vs Ag/AgCl. However, this reduction overlaps exactly with the n-doping region of PBTh and as a result, we were unable to study the HER reduction on PBTh in the dark as it becomes severely obscured by the n-doping region of the polymer.

This finding meant the continued reliance on external light sources and ruled out highly photosensitive techniques like transient absorption spectroscopy. Furthermore, it was clear that the photo-excitation of PBTh created notably different thermodynamic and electronic conditions for the HER.

5 Computational Studies

5.1 Use of 7-membered "polythiophene"

The $\nu_1 : \nu_2$ ratio of sexithiophene was compared to that of the VPP PBTh as a measure of conjugation and thus, chain length. Higher ratios indicate a higher percentage of central thiophene rings and thus, longer chain lengths; the measure is crude but the insoluble nature of PBTh prevents more accurate methods. A Gaussian function was used to fit the two peaks and the corresponding peak area and ratio given, Figure S12.

The relatively close $\nu_1 : \nu_2$ ratio suggests that the PBTh film has a similar conjugation length to that of sexithiophene, thus supporting our use of a 7-membered thiophene analogue. Nevertheless, it again must be stressed that this a tentative relationship, particularly given the lack of data on how the $\nu_1 : \nu_2$ ratio varies with chain length.

An 8-membered ring could arguably fit this trend even better – given that *bi*thiophene was the starting monomer – however a symmetry around the active central thiophene ring was preferred. A more accurate determination of chain length using techniques such as chromatography, light scattering or even mass spectroscopy was not possible due to the insoluble nature of PBTh.
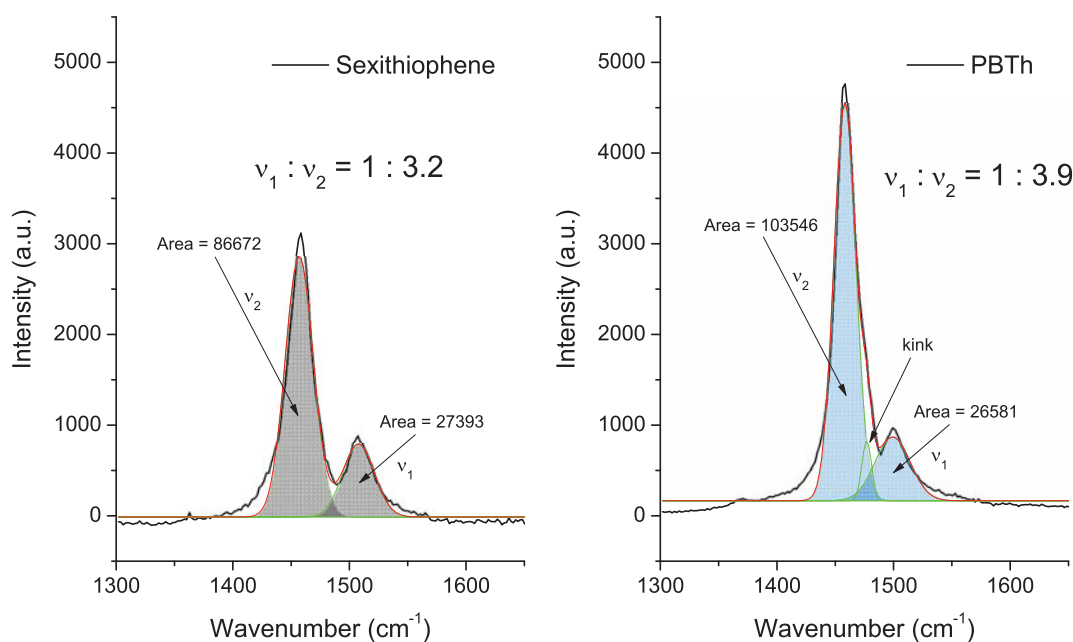

Figure S12: Comparison of the $\nu_1 : \nu_2$ ratio in sexithiophene (left) and PBTh (right)

We emphasize that this computational model represents a preliminary, gas phase, non-solvated and thermodynamic study. Kinetic investigations were not attempted as they are costly and highly variable depending on the assumptions of the system; this was of particular issue given the lack of robust experimental data.

5.2 Further Triplet state analysis of PBTh

The T_1 state of PBTh (Figure S13C) shows a much more restricted electron cloud and does not present a favourable site for protonation. In comparison, the S_1 state (Figure S13B) shows a larger, more diffuse MO, over the sulphur atom which would aid in the success of protonation. Hence supporting that the first protonation occurs via the *singlet* excitation of PBTh and subsequent localised charge transfer to H^+ at the sulphur site to form PBTh(S-H)$^+$.
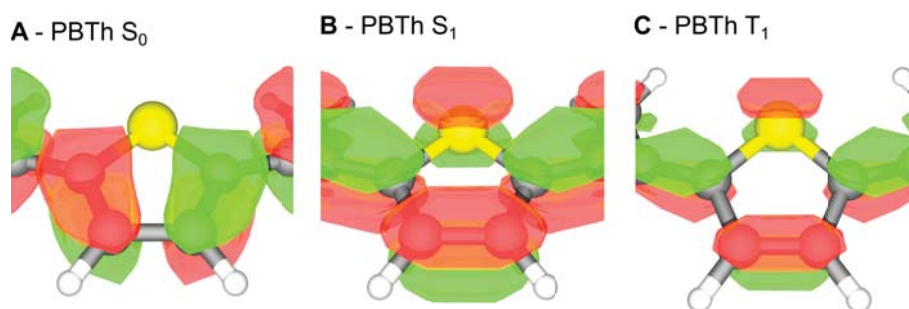

Figure S13: The triplet state (T_1) of PBTh as compared to the ground singlet (S_0) and excited singlet (S_1) states.

6 Proposed Mechanism

The final mechanism remains highly contested. Regardless, from the data currently available to us, we propose the reaction mechanism as shown in Figure S14 which places a heavy emphasis on a photo-driven mechanism. For completeness, other possible pathways are also presented as they have not yet been conclusively ruled out. It is even possible that all the proposed mechanisms may be occurring simultaneously.
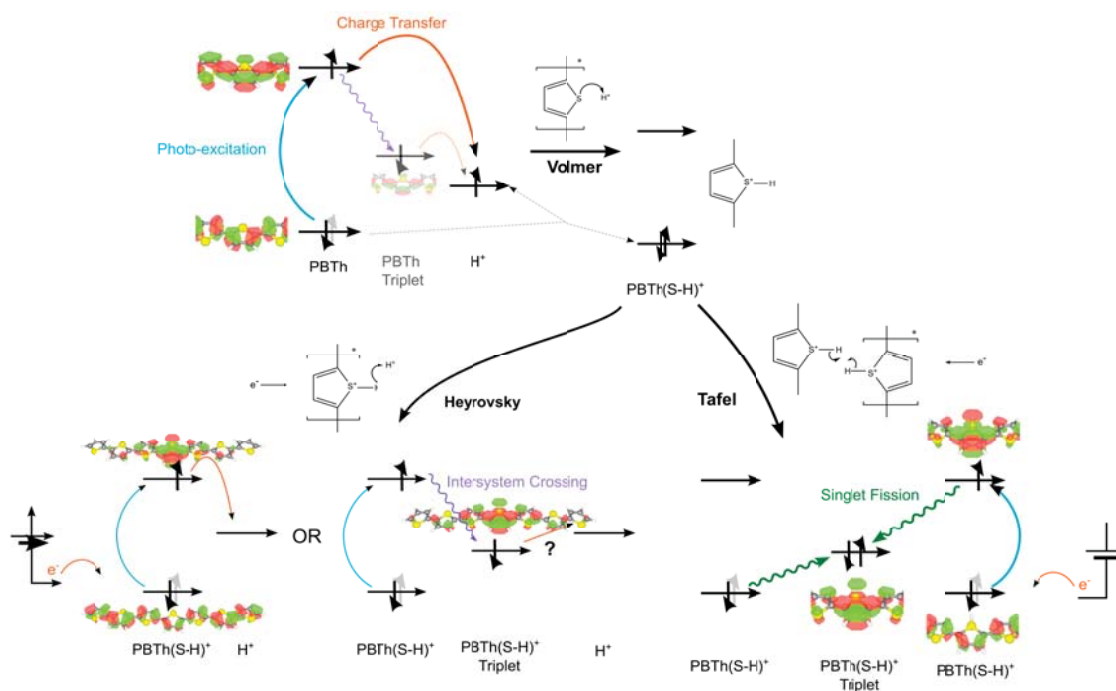

Figure S14: The proposed mechanism is presented (solid colours); the band positions are taken from single point energy calculations of the respective species. Although these energies are not quantitative, it gives a starting point for the relative positions and furthermore, show good thermodynamic agreement with the proposed scheme. It should be noted, as discussed in the main text that these proposed mechanisms are by no means confirmed but simply one possible explanation for observed data and trends.